The Astrophysical Journal, 938:134 (11pp), 2022 October 20 https://doi.org/10.3847/1538-4357/ac892f

HST UV Spectroscopy of the Planet-hosting T Tauri Star PDS 70

Stephen L. Skinner[1] and Marc Audard[2]
[1] Center for Astrophysics and Space Astronomy (CASA), University of Colorado Boulder, Boulder, CO, USA 80309-0389; stephen.skinner@colorado.edu
[2] Department of Astronomy, University of Geneva, Ch. d'Ecogia 16, 1290 Versoix, Switzerland
Received 2022 July 6; revised 2022 August 5; accepted 2022 August 10; published 2022 October 20

Abstract

We summarize Hubble Space Telescope (HST) UV observations of the weak-lined T Tauri star (wTTS) PDS 70 obtained with the Space Telescope Imaging Spectrograph. These observations provide the first far-UV (FUV) and near-UV (NUV) spectra of PDS 70. Ground-based observations have so far revealed two formative giant planets orbiting in a wide gap in its circumstellar disk. Both the star and young planets are thought to still be accreting. The HST spectra provide new insight into physical conditions in the star's outer atmosphere and circumstellar environment. The spectra are dominated by chromospheric and transition-region emission lines with maximum formation temperatures log $T = 4.5$–5.2 K. Stellar continuum emission is present in the NUV but we find no significant FUV continuum, as could arise from accretion shocks. Several fluorescent FUV H_2 emission lines are present, a surprising result since H_2 lines are usually undetected in wTTS. The H_2 lines likely originate in irradiated circumstellar gas that could serve as a reservoir for the star's waning accretion. A previously established correlation between C IV line luminosity and accretion rate yields $\dot{M}_{\rm acc} \sim 10^{-10}\,M_\odot\ {\rm yr}^{-1}$, consistent with previous estimates. Atacama Large Millimeter/submillimeter Array disk gas models imply strong absorption of stellar X-ray and UV (XUV) radiation near the star, effectively shielding the planets. Inner disk gas is exposed to ongoing photoevaporation by XUV radiation and the disk is nearing the end of its expected lifetime, making PDS 70 an important example of a young planet-hosting star in the late stage of accretion.

Unified Astronomy Thesaurus concepts: Pre-main sequence stars (1290); Ultraviolet astronomy (1736); Weak-line T Tauri stars (1795)

1. Introduction

In a remarkable discovery, Keppler et al. (2018, 2019) reported the direct detection of a giant protoplanet, named PDS 70b, orbiting the ∼5 Myr old T Tauri star (TTS) PDS 70 (Table 1). It was detected at a projected angular separation ≈0.″195 (≈22 au) from the star and lies within a wide dust-depleted gap in the circumstellar disk. The existence of PDS 70b was confirmed by Haffert et al. (2019), who also reported the detection of a second giant protoplanet, PDS 70 c, at a projected angular separation ≈0.″24 (≈27 au). Assuming that the planets move in circular orbits in the circumstellar disk and a disk inclination $i_{\rm disk} = 49.^\circ7$, Haffert et al. computed deprojected orbital radii of ≈21–22 au (PDS 70b) and ≈34–40 au (PDS 70c). Their estimated masses are 4–17 $M_{\rm Jup}$ (PDS 70b) and 4–12 $M_{\rm Jup}$ (PDS 70c). Both protoplanets were detected at Hα and submillimeter wavelengths and are thought to still be accreting from circumplanetary disks at low rates of $(1\text{–}2) \times 10^{-8}\ M_{\rm Jup}\ {\rm yr}^{-1}$ (Christiaens et al. 2019; Haffert et al. 2019; Isella et al. 2019; Zhou et al. 2021). Active accretion implies the planets are still in the formative stage.

Previous studies have reached different conclusions as to whether the star itself is still accreting. PDS 70 was classified as a weak-lined T Tauri star (wTTS) on the basis of its Hα equivalent width (EW) by Gregorio-Hetem & Hetem (2002). Generally, accretion from circumstellar disks is believed to have ceased in wTTSs (or dropped below detectable levels) but Hα EW alone does not provide a reliable accretion indicator (Johns-Krull et al. 2000). Using Swift UV filter fluxes, Joyce et al. (2020) concluded that the UV emission of PDS 70 is mainly chromospheric, and derived an accretion rate no larger than log $\dot{M}_{\rm acc} = -11.22$ $M_\odot\ {\rm yr}^{-1}$. Using Atacama Large Millimeter/submillimeter Array (ALMA) observations obtained in 2016 with a synthesized beam of ≈0.″17, Long et al. (2018) found no significant gas inside of 1 au, suggesting that the star is not actively accreting. But Haffert et al. (2019) noted that the *stellar* Hα line has an inverse P-Cygni profile showing redshifted absorption, which usually signifies accretion in TTSs. Furthermore, disk models analyzed by Manara et al. (2019) found PDS 70 to be accreting at a rate log $\dot{M}_{\rm acc} = -10.26\ M_\odot\ {\rm yr}^{-1}$. More recently, Thanathibodee et al. (2020) modeled the Hα line profile of PDS 70 and concluded that the star is still accreting at a variable rate log $\dot{M}_{\rm acc} = (-10.22 - -9.66) M_\odot\ {\rm yr}^{-1}$. They also detected blueshifted absorption in the He I line (10830 Å) at a velocity $v \approx -85$ km s^{-1}, indicating a wind that may originate in the inner disk. Considering the above results together, it seems likely that the star is still accreting but at lower rates than typically inferred for accreting classical TTSs (cTTSs) of similar K7 spectral type (Ingleby et al. 2013).

UV spectra provide an excellent diagnostic for characterizing physical conditions in the star's chromosphere and transition region, identifying accretion signatures such as near-UV (NUV) or far-UV (FUV) excess continuum emission, and searching for fluorescent H_2 emission from molecular gas near the star that could serve as an accretion reservoir. No UV spectra of PDS 70 have been obtained in previous work but some information on UV fluxes and X-ray emission was provided by Swift (Joyce et al. 2020). Swift obtained NUV fluxes in two broadband filters, namely the *uvw*1 filter (2253–2946 Å) and *uvw*2 filter (1599–2256 Å). These filters capture continuum and line emission, both of which are expected to be present in a K7-type TTS. For example, the

Table 1
PDS 70 Stellar Properties

Sp. type	Age (My)	M_* ($M_\odot$)	R_* ($R_\odot$)	L_* ($L_\odot$)	$T_{\rm eff}$ (K)	V (mag)	A_V (mag)	RV (km s^{-1})	d (pc)
K7IVe (1,2)	5.4 ± 1.0 (3)	0.76 (3)	1.26 (1,3)	0.35 (1,5)	3972 ± 37 (1,2)	12.2 (4)	$0.05^{+0.05}_{-0.03}$ (3)	3.13 ± 1.4 (6)	112.39 ± 0.24 (7)

Note. References: (1) Pecaut & Mamajek (2016); (2) Gregorio-Hetem & Hetem (2002). give spectral type K5 and $T_{\rm eff} = 4406$ K; (3) Müller et al. (2018); (4) Kiraga (2012); (5) Keppler et al. (2018); (6) Radial velocity (RV): Gaia DR2, a value RV $= 6.0 \pm 1.5$ km s^{-1} was obtained by Thanathibodee et al. (2020); (7) Distance: Gaia EDR3.

Table 2
HST STIS/MAMA First-order UV Grating Observations of PDS 70

Grating	Start (UT)	λ range[a] (Å)	Resolving Power[b]	Dispersion $\Delta\lambda$ (Å/pixel)	Scale ($''$/pixel)	Exposure (s)	Total Time (s)
G230L (NUV)	2020-12-29 11:09	1570–3180 (2376)	500-1010	1.58	0.025	739 (×3)	2217
G140L (FUV)	2020-12-29 12:37	1150–1730 (1425)	960-1440	0.60	0.025	887 (×3)	2661

Notes. The observations were centered on PDS 70 using target coordinates (J2000) R.A. $= 14^{\rm h}\,08^{\rm m}\,10.154^{\rm s}$, Decl. $= -41°\,23'\,52\farcs58$. All exposures were obtained in ACCUM mode with the $52'' \times 0\farcs2$ slit. Target acquisition was performed using a 0.4 s STIS CCD image taken through the F28X50LP long-pass filter. Grating properties are from the STIS Instrument Handbook.
[a] Central wavelength in parentheses.
[b] Resolving power $= \lambda/(2\Delta\ \lambda)$.

*uvw*1 filter includes strong lines such as the Mg II doublet (2297/2804 Å). In order to distinguish between the separate line and continuum contributions to the total flux, UV spectra are required. In addition, Swift filters do not cover the FUV range below 1600 Å, which includes important diagnostic lines such as the C IV resonance doublet (1548/1551 Å) and many H_2 transitions.

The proximity and low visual extinction of PDS 70 make it a superb candidate for UV spectroscopy since large uncertainties associated with dereddening are mitigated. Because of its importance as a young planet-hosting star that may still be accreting at low rates, we obtained high-quality Hubble Space Telescope (HST) near-simultaneous FUV and NUV grating spectra of PDS 70 in 2020 December. These spectra characterize the stellar UV continuum and line emission of PDS 70 for the first time and reveal fluorescent H_2 emission lines originating in circumstellar molecular gas.

2. Observations and Data Reduction

The HST Space Telescope Imaging Spectrograph (STIS) long-slit observations of PDS 70 were obtained during two consecutive orbits on 2020 December 29 using the Multi-Anode Micro-channel Array (MAMA) detectors. NUV and FUV spectra were obtained using the low-resolution G230L and G140L gratings, respectively. Three exposures of equal length were obtained for each grating. Table 2 summarizes the observations and basic instrument properties. Data were analyzed using PyRaf v. 2.1.6 and IRAF v. 2.7. Calibrated one-dimensional spectral files (x1d.fits) for the individual exposures provided by the STIS pipeline were combined into a single spectrum for each grating using tools in the Space Telescope Data Analysis System (STSDAS). Spectral fitting and line property measurements were undertaken using STSDAS tools. Fluxes were dereddened using the extinction law of Whittet et al. (2004) assuming $A_V = 0.05$ mag for PDS 70.

3. Results

3.1. Acquisition Image

Target acquisition was performed using a STIS CCD image with a 0.4 s exposure taken through the long-pass F28X50LP filter. This filter spans a wavelength range ≈5400–10000 Å with maximum sensitivity over 6000–7400 Å. The raw acquisition image near PDS 70 is shown in Figure 1. In addition to PDS 70 a second faint source is visible at an offset of $\approx 2\farcs5$ along P.A. $\approx 14°$. This source is found in the Gaia Early Data Release 3 (EDR3) catalog at magnitude $G = 15.504$, about 4 mag fainter than PDS 70 ($G = 11.606$). The Gaia EDR3 parallax of the faint source is 0.042 ± 0.038 mas, nearly consistent with zero. Its small parallax and apparent faintness suggest it is a distant background object. This faint source was not captured in the STIS grating slit (aperture P.A. $= -134\fdg35$) and did not affect the UV spectra.

3.2. UV Spectra

The STIS FUV and NUV spectra obtained by combining the individual exposures are shown in Figure 2. Prominent emission lines are marked and measured line fluxes are summarized in Tables 3 and 4 along with selected NUV continuum flux density measurements taken over narrow wavelength intervals where no obvious lines are visible or listed in the Chianti Atomic Database.[3]

3.2.1. Continuum

Since PDS 70 is a late-type (K7) pre-main-sequence star, UV continuum emission is anticipated from the stellar atmosphere. This will include photospheric emission that peaks in the visible range but extends downward into the NUV plus continuum from hotter chromospheric and transition-region plasma in the upper atmosphere. A question of interest is whether excess continuum emission is present in addition to

[3] https://www.chiantidatabase.org

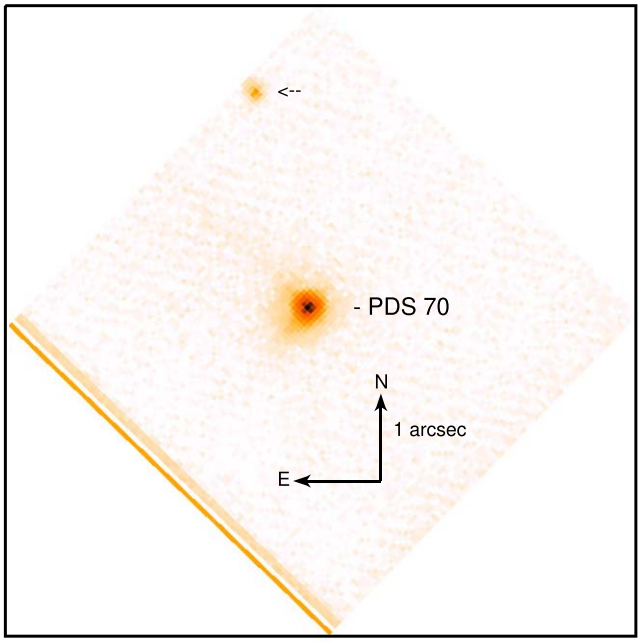

Figure 1. Raw STIS CCD acquisition image of PDS 70 taken through the F28X50LP filter showing a second faint source (Gaia EDR3 source_id 6110141563309613184) located ≈2.″5 northeast of PDS 70.

that of the star's atmosphere. Excess UV continuum is often seen in cTTSs and is usually attributed to an accretion shock (Johns-Krull et al. 2000; Ingleby et al. 2013). In addition, collision and excitation of H_2 by energetic electrons can give rise to FUV continuum emission via H_2 dissociation (Bergin et al. 2004; France et al. 2011). However, even in accreting cTTSs any NUV continuum emission originating in an accretion shock is not easily distinguished from that of hot plasma in the star's upper atmosphere, as discussed by Kravtsova & Lamzin (2003).

Figure 3 shows *dereddened* continuum flux density measurements of PDS 70 in narrow wavelength intervals where no emission lines are visible or listed in the Chianti Atomic Database. Dereddening has very little effect assuming $A_V = 0.05$ for PDS 70. The photospheric continuum is clearly detected in the NUV and a power-law fit extrapolates to zero photospheric flux density at ≈2545 Å. This cutoff is consistent with predictions of stellar photosphere models for K7 spectral type, e.g., the Pickles K7V ($T_{\rm eff} = 3999$ K) template in the STIS Exposure Time Calculator. Taking the ratio of the dereddened photospheric continuum flux densities at different wavelengths (Table 3) yields an estimate of the equivalent NUV-derived blackbody temperature $T_{\rm eff(nuv)}$. Specifically, F_{2922}/F_{3077} gives $T_{\rm eff(nuv)} = 4007$ K and F_{2875}/F_{3077} gives a slightly higher value $T_{\rm eff(nuv)} = 4048$ K. These values are within 1%–2% of the value $T_{\rm eff} = 3972 \pm 37$ K obtained by Pecaut & Mamajek (2016). This agreement is reasonably good considering that STIS flux density measurements at the above wavelengths are uncertain by 3%–5% and A_V is uncertain by a factor of 2 (Table 1).

Significant NUV continuum is also present in the 1795–2561 Å range below the photospheric cutoff. But at the high end of this range (≈2330–2550 Å) no reliable continuum measurements were obtained due to many closely spaced emission lines that cannot be individually identified at the resolution of G230L, especially Fe II transitions. Faint emission that *may* be weak continuum is also measured in the FUV over the range 1282–1515 Å. However, any real FUV continuum emission that may be present is of low significance. Figure 4 compares the gross, net, and background count rates over a narrow FUV wavelength interval (1453–1454.9 Å) where no emission lines are present. The ratio of gross (source + background) to background rates is $2.2/1.2 = 1.8$, which is too low to qualify as a significant continuum detection. But we do note here that near-constant FUV continuum emission has been reported in some accreting cTTSs (Kravtsova & Lamzin 2003; France et al. 2014).

In summary, the NUV continuum emission of PDS 70 longward of ≈2600 Å is dominated by the star's photosphere. Below this cutoff the NUV continuum is dominated by hotter thermal plasma from the star's chromosphere and transition region. Any excess FUV continuum emission that might be present is too faint to be clearly distinguished from MAMA background.

3.2.2. Emission Lines

Measured line centroids agree with lab wavelengths to within the absolute STIS wavelength accuracies, but many of the detected lines are closely spaced blends that are not clearly separated by the low-resolution STIS gratings. Maximum line power temperatures (Table 3) lie within the range log $T_{\rm max} = 4.5$–5.2 (K) as is typical for chromospheric and transition-region plasma. The lines with the highest $T_{\rm max}$ are the N V and Ne IV lines. The feature identified as Ne IV (1601.45 Å) is quite faint and thus classified as a possible detection. The brightest lines are the blended C IV doublet in G140L and the Mg II doublet in G230L. Density-sensitive carbon lines are discussed further below (Section 3.4).

The H I Lyα line (1215.7 Å) is also brightly detected but is adversely affected by Earth's geocoronal emission and interstellar absorption (resonant scattering of photons out of the line of sight). Reconstructing the intrinsic Lyα line and its flux from the observed line requires HST medium resolution or echelle grating spectra capable of resolving the line profile (e.g., Wood et al. 2005; Youngblood et al. 2022). The low-resolution G140L spectrum analyzed here is insufficient for this purpose.

We compared the C IV doublet lines of the three exposures (Figure 5) to determine if any significant flux variability occurred. Only small differences were found with, at most, a ±6% variation in the integrated C IV doublet flux for the individual exposures compared to their mean value. The measured (absorbed) C IV line flux in the combined spectrum and range for the three exposures was $F_{\rm CIV}$ (1548+1550) = 1.33 (1.29–1.44) × 10^{-14} ergs cm^{-2} s^{-1}.

H_2 lines. Somewhat surprisingly, a search of the G140L spectrum at several wavelengths where fluorescent H_2 lines are often detected in accreting cTTSs revealed five faint H_2 emission lines as identified in Figure 6 and Table 4. Other known H_2 lines whose lab wavelengths lie in the wings of bright lines such as C IV may also be present but cannot be distinguished at G140L spectral resolution. The presence of H_2 lines in the UV spectra of cTTSs is thought to be due mainly to excitation of H_2 near the star radiatively pumped by stellar Lyα photons and subsequent fluorescent deexcitation (Ardila et al. 2002). Although most cTTSs observed with HST FUV gratings show fluorescent H_2 lines, their detection in wTTSs is rare. All five H_2 lines in the PDS 70 spectrum have the same vibrational

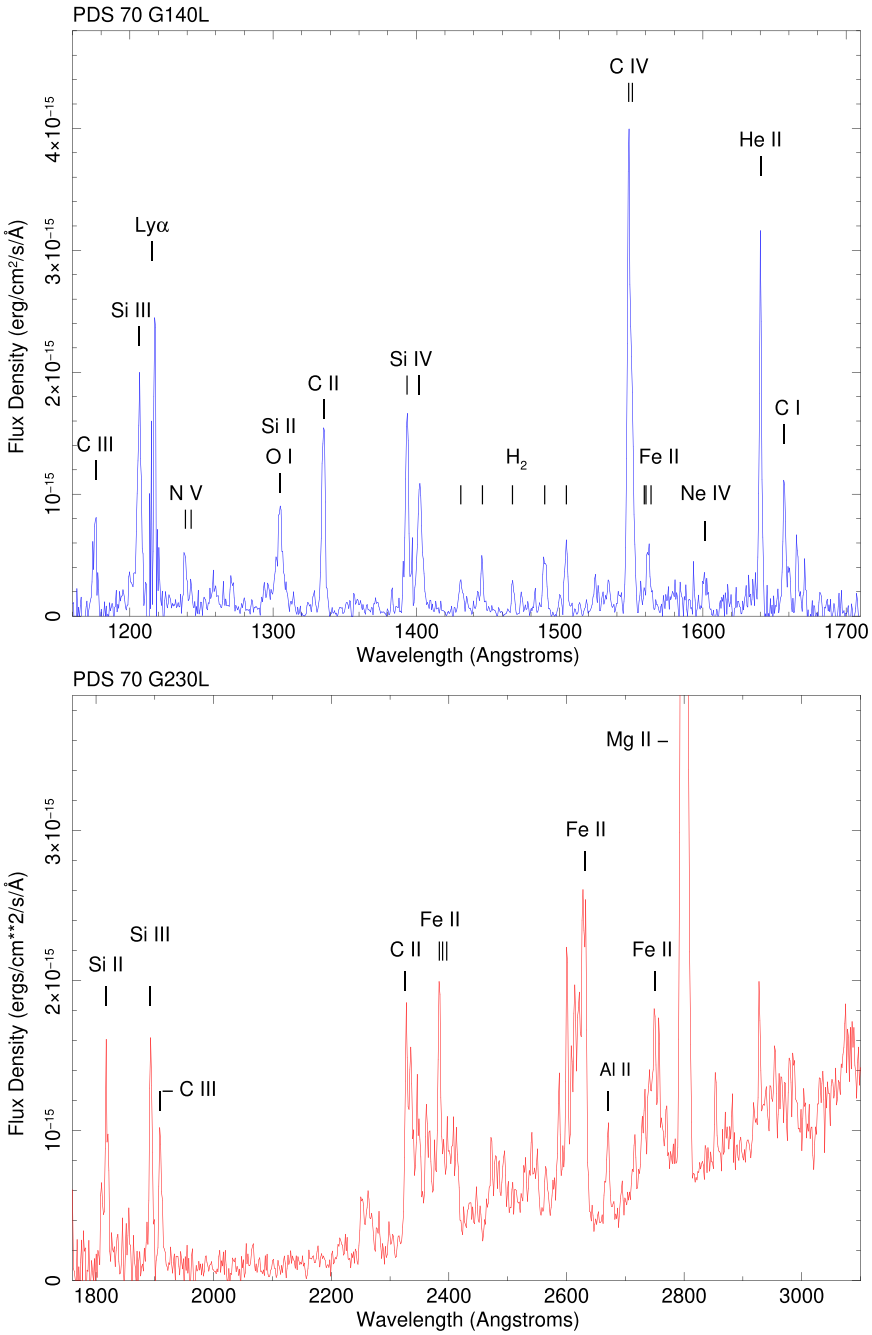

Figure 2. STIS/MAMA G140L and G230L spectra of PDS 70 from the combined exposures with prominent emission lines identified. The O I line in G140L is geocoronal.

quantum number ($v' = 1$) for the excited electronic state and all but one have the same rotational quantum number ($J' = 4$) for the excited state. The dereddened line fluxes are low compared to typical values for cTTSs (e.g., Figure 5 of France et al. 2012 for [1,4] transitions).

The detection of H_2 lines provides evidence for molecular gas in the vicinity of the star and STIS provides a moderate constraint on its spatial extent. As a check for extended H_2 emission we extracted G140L spectra centered at offsets as close as ± 12 pixels ($\pm 0\farcs30$) from the stellar trace using the MAMA default extraction width of 11 pixels ($\pm 0\farcs14$) in the spatial direction. At the distance of PDS 70 an offset of $0\farcs30 \pm 0\farcs14$ corresponds to a projected separation of 34 ± 16 au. No significant H_2 emission was seen in these off-source spectra at the wavelengths where on-source H_2 lines are visible. Thus the H_2 lines originate within a projected separation of $\leqslant 34$ au from the star. This region contains the planets, part of the dust-depleted gap, the region at <10 au where an inner disk may be present (Long et al. 2018; Keppler et al. 2019), and, of course, the star itself.

To place tighter constraints on the location of the H_2 emission in PDS 70 a more sensitive FUV observation using higher-spatial-resolution imaging or higher-spectral-resolution gratings capable of accurately measuring line centroids and resolving line shapes and widths is needed. If the H_2 emission originates in the disk close to the star then line centroid shifts should be negligible and excess line broadening from gas orbiting in the disk is expected. For H_2 emission originating in a molecular outflow significant line centroid shifts relative to

Table 3
PDS 70 UV Emission Lines

Grating	Name	λ_{lab}[a] (Å)	λ_{obs}[b] (Å)	log T_{max}[a] (K)	Flux[b] (10^{-15} erg cm^{-2} s^{-1})
G140L	C III	1176.37	1176.5	4.8	2.42
G140L	Si III	1206.50	1206.6	4.7	5.39
G140L	C III	1247.38	⋯	4.9	⩽0.08
G140L	N V	1238.82, 1242.81	1238.6	5.2	1.62[c]
G140L	Si II, O I[d]	1304.37,1304.86	1304.7	4.5	4.17
G140L	C II	1334.53,1335.71	1335.2	4.5	4.73
G140L	Si IV	1393.76	1393.5	4.9	4.57
G140L	Si IV	1402.77	1402.4	4.9	4.16
G140L	C IV	1548.19+1550.78	1548.7	5.0	13.3[c]
G140L	Fe II	1560.25, 1563.79	1561.8	4.5	2.4
G140L	Ne IV ?	1601.45	1601.49	5.2	0.9
G140L	He II	1640.34,1640.54	1640.2	4.9	5.83
G140L	C I	1656.93,1657.008[e]	1656.9	⋯	2.64
G230L	Si II	1816.93, 1817.45	1817.2	4.5	5.79
G230L	Si III	1892.03	1893.0	4.6	7.94
G230L	C III	1908.73	1909.1	4.8	5.00
G230L	C II	2326.12, 2327.65	2327.9	4.5	7.93
G230L	Fe II	2629.09, 2632.11	2629.3	4.5	20.5
G230L	Al II	2669.95	2670.1	4.5	3.10
G230L	Mg IIk	2796.35	2797.2	4.5	104.0
G230L	Mg IIh	2803.53	2804.0	4.5	70.8
G230L	Continuum	⋯	2077.7 ± 2.4	⋯	0.109 (0.125)[f]
G230L	Continuum	⋯	2875.3 ± 4.2	⋯	0.960 (1.047)[f,g]
G230L	Continuum	⋯	2921.9 ± 2.4	⋯	1.074 (1.170)[f,g]
G230L	Continuum	⋯	2970.0 ± 2.5	⋯	1.221 (1.328)[f,g]
G230L	Continuum	⋯	3077.5 ± 2.5	⋯	1.550 (1.682)[f,g]

Notes.
[a] Lab wavelengths and maximum line power temperatures are from the Chianti Atomic Database (www.chiantidatabase.org) unless otherwise noted.
[b] Measured wavelengths and observed line fluxes are based on Gaussian fits and line fluxes are continuum subtracted. STIS MAMA absolute wavelength accuracy is 0.5–1.0 pixel, or 0.3–0.6 Å (G140L) and 0.8–1.6 Å (G230L). For continuum measurements the wavelength uncertainty specifies the range over which the mean flux density was measured.
[c] Sum of the two components based on a two-component Gaussian fit.
[d] O I is geocoronal.
[e] Lab wavelengths from NIST (https://physics.nist.gov/PhysRefData/Handbook/Tables/carbontable2.htm).
[f] Mean of the observed flux density (units: 10^{-15} erg cm^{-2} s^{-1} Å^{-1}) over the specified wavelength interval followed in parentheses by dereddened values computed using the extinction law of Whittet et al. (2004) and $A_V = 0.05$.
[g] Flux density is dominated by photospheric continuum.

Table 4
PDS 70 H_2 FUV Emission Lines

Grating	Transition[a]	[ν', J']	λ_{lab} (Å)	λ_{obs} (Å)	λ_{pump} (Å)	Flux[b] (10^{-15} erg cm^{-2} s^{-1})
G140L	R(3) 1–6	[1,4]	1431.01	1431.1	1216.07	0.86 (0.97)
G140L	R(3) 1–7	[1,4]	1489.57	1489.6	1216.07	1.45 (1.64)
G140L	P(5) 1–6	[1,4]	1446.12	1445.8	1216.07	1.02 (1.15)
G140L	P(5) 1–7	[1,4]	1504.76	1504.6	1216.07	1.30 (1.46)
G140L	P(8) 1–6	[1,7]	1467.08	1467.3	1215.73	0.53 (0.60)

Notes.
[a] H_2 transitions are in the Lyman band system (Abgrall et al. 1993). Vibrational and rotational quantum numbers in the upper electronic state are [ν', J'] and in the lower electronic state [ν'', J'']. The letter "P" denotes $\Delta J = -1$ and "R" denotes $\Delta J = +1$, where $\Delta J = J' - J''$. The number in parentheses is J''. The two hyphenated numbers are the vibrational quantum numbers $\nu' - \nu''$ in the upper and lower electronic states.
[b] Observed fluxes are followed in parentheses by dereddened values computed using the extinction law of Whittet et al. (2004) and $A_V = 0.05$.

the stellar radial velocity are anticipated. Stellar H_2 lines (e.g., from cool spots) would be unshifted with broadening consistent with $v\sin i$.

In HST Cosmic Origins Spectrograph and STIS FUV grating observations of a sample of disked cTTSs by France et al. (2012), most stars revealed H_2 lines broadened to FWHM

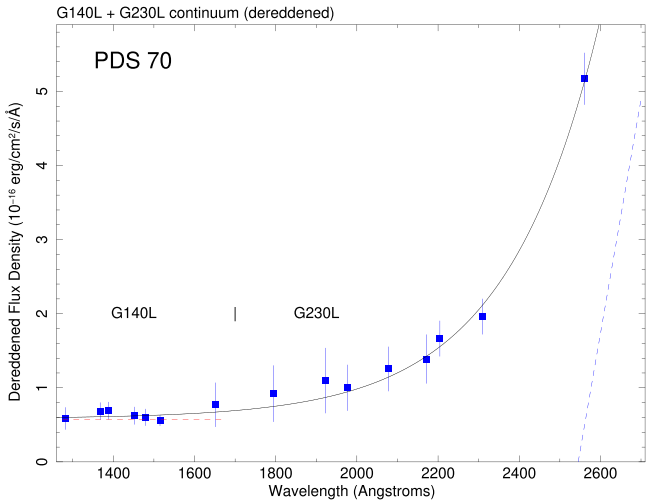

Figure 3. PDS 70 G140L and G230L continuum flux densities measured in narrow wavelength intervals and dereddened using $A_V = 0.05$ and the extinction law of Whittet et al. (2004) Flux densities are in units of 10^{-16} erg cm^{-2} s^{-1} Å^{-1} . The sloping blue line at far right is a power-law fit to four dereddened photospheric continuum measurements (Table 3) $F_{\lambda,\rm dered} = -101.5 + 0.1947\lambda^{+0.7978}$ extrapolated to zero flux density at $\lambda = 2545$ Å . The red dashed line at left shows the mean FUV MAMA background level (no dereddening) at $F_{\lambda,\rm bgd} = 5.42 \times 10^{-17}$ erg cm^{-2} s^{-1} Å^{-1} . The curved line is a fit of 15 continuum data points (1282–2561 Å) using an exponential model with a constant offset of the form $F_{\lambda,\rm dered} = C + A\exp[(\lambda - \lambda_0)/\rm EW$. Best-fit values are $C = 0.5836$, $A = 0.2908$, EW = 230.7, $\lambda_0 = 1926$. The data and model become indistinguishable from background at $\lambda < 1600$ Å .

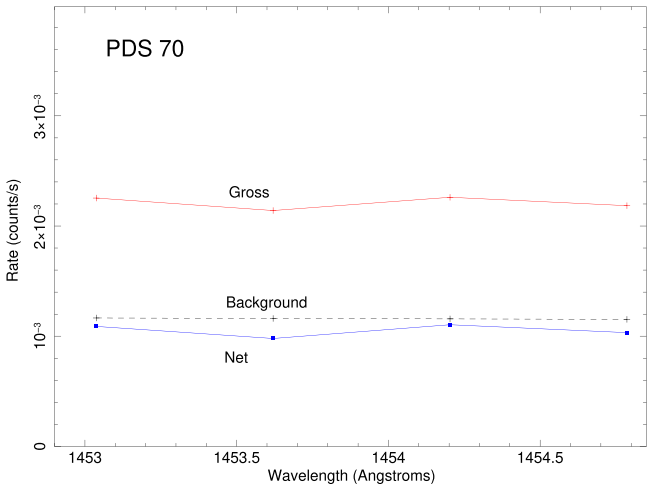

Figure 4. PDS 70 G140L gross (=source + background), net (=source − background), and background count rates from the combined exposures in a narrow wavelength interval where no significant line emission is expected. The background rate is based on the average of two background spectra extracted at offsets of ±300 pixels (±7.″5) from the stellar trace. Source and background rates were measured in spectra extracted with a width of 11 pixels in the cross-dispersion (spatial) direction.

≈20–90 km s^{-1} with little or no velocity shifts. They concluded that the H_2 emission of these stars arises in the disk at small separations of $\lesssim$3 au. Similarly, some cTTSs in the sample observed with STIS by Herczeg et al. (2006) showed H_2 lines centered on the star's radial velocity. But a few cTTSs in the France et al. and Herczeg et al. samples and of those observed by Ardila et al. (2002) revealed H_2 lines blueshifted up to a few tens of kilometers per second, indicative of low-velocity molecular outflows. Blueshifted H_2 FUV lines were also detected in STIS observations of the jet-driving cTTS RY Tau by Skinner et al. (2018). Wide-angle H_2 FUV emission that may arise in a disk wind was also reported for the jet-driving cTTS DG Tau by Schneider et al. (2013a, 2013b). Taken together, the above results suggest that different regions contribute to fluorescent H_2 emission in cTTSs, and models that incorporate both disks and molecular outflows are required to explain the observations.

3.3. UV Luminosity

FUV and NUV. The FUV luminosity is dominated by line emission. To compute $L_{\rm FUV}$ we exclude Lyα (1216 Å) and O I (1304.9+1306.0 Å) since Lyα is heavily absorbed by the interstellar medium and both lines are contaminated by geocoronal emission.[4] Dereddening the other FUV line fluxes in Table 3 and summing gives $L_{\rm FUV,line}(1170–1700\ \text{Å}) = 8.54 \times 10^{28}$ erg s^{-1}. The largest contributor is the C IV doublet, with a dereddened flux $F_{\rm Civ,dered}(1548+1551) = 1.50 \times 10^{-14}$ erg cm^{-2} s^{-1} and $L_{\rm Civ} = 2.26 \times 10^{28}$ erg s^{-1}. If the near-constant exponential tail of the FUV continuum flux density fit below 1700 Å shown in Figure 3 is included but treated as an upper limit to the FUV continuum then $L_{\rm FUV,line+cont}(1170–1700\ \text{Å}) \leqslant 1.43 \times 10^{29}$ erg s^{-1}. The NUV luminosity is dominated by the continuum, especially above 2600 Å where the stellar photosphere begins to contribute significantly. Thus, the value obtained for $L_{\rm NUV}$ depends sensitively on the wavelength adopted for the upper limit in the calculation. Using an upper limit of 3000 Å gives $L_{\rm NUV,line+cont}(1700–3000\ \text{Å}) = 1.2 \times 10^{30}$ erg s^{-1}. The Mg II doublet contribution is $L_{\rm MgII}(2797+2804) = 2.88 \times 10^{29}$ erg s^{-1}.

EUV. Direct measurements of the extreme-UV (EUV) flux and luminosity (0.013–0.1 keV) are only possible for the Sun and a few nearby stars due to insterstellar absorption. But methods for estimating $L_{\rm EUV}$ in late-type stars have been proposed using L_X as a reference. For the solar-like star EK Dra (age ∼70 Myr) a ratio $L_{\rm EUV}/L_X \approx 1$ was found by Ribas et al. (2005). Analysis of a large sample of mature, late-type stars of ages $\gtrsim$100 Myr by Sanz-Forcada et al. (2011) provided a relation between $L_{\rm EUV}$ and L_X but with large uncertainties in the fit coefficients. Applying their fit to PDS 70 gives $L_{\rm EUV}/L_X \approx 4$. A similar ratio was obtained using the theoretical relations between $L_{\rm EUV}$, L_X, and age developed by Tu et al. (2015). These estimates are subject to the caveat that the relations of Sanz-Forcada et al. and Tu et al. are not well constrained observationally for young stars with ages $\lesssim$30 Myr such as TTSs. Scaling relations of L_X with age or rotation rate break down in young, rapidly rotating stars when coronal X-ray emission saturates at high levels of magnetic activity. X-ray saturation occurs at $L_X \approx 10^{-3}\ L_*$ (Güdel et al. 1997).

Swift X-ray observations of PDS 70 analyzed by Joyce et al. (2020) obtained an intrinsic (unabsorbed) X-ray flux $F_{X,\rm int}(0.3–10\ \text{keV}) = 3.4 \times 10^{-13}$ erg cm^{-2} s^{-1} or log $L_X =$ 29.71 erg s^{-1} at a distance of 112.39 pc. More extensive XMM-Newton observations in mid-2020 show that the X-ray luminosity of PDS 70 is variable and increases by a factor of ∼3 or more during periods of high activity. During low-activity states (e.g., ObsIDs 0863800201 and 0863800401), our fits of archived XMM-Newton European Photon Imaging Camera pn spectra give $F_{X,\rm int}(0.2–7.5\ \text{keV}) \approx 4.18 \times 10^{-13}$ erg cm^{-2} s^{-1},

[4] https://www.stsci.edu/itt/APT_help/STIS_Cycle22/c06_exptime6.html

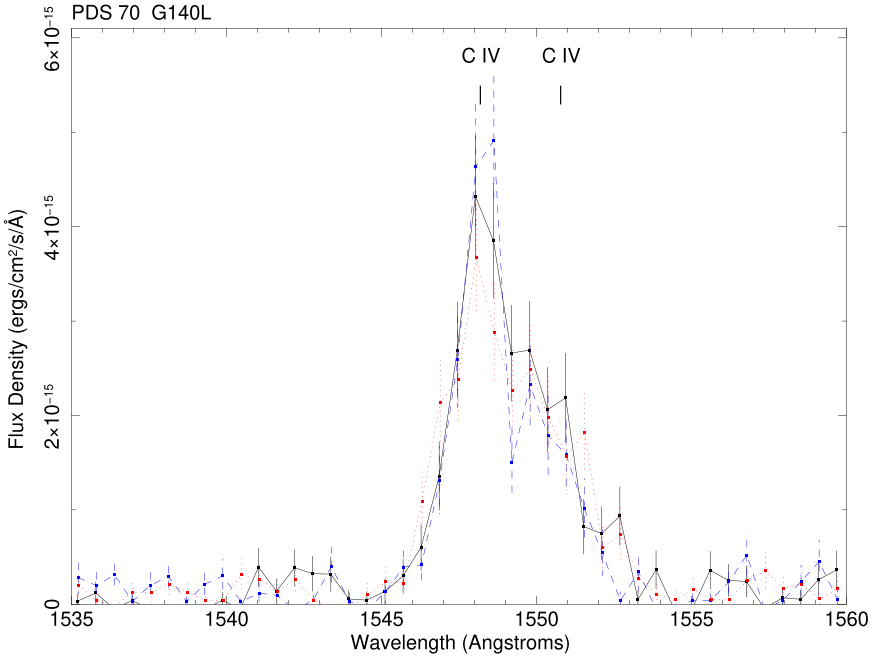

Figure 5. STIS/MAMA G140L spectra of PDS 70 for the three exposures showing the C IV doublet ($\lambda_{lab} = 1548.19, 1550.78$ Å). Solid black: exposure 1; dashed blue: exposure 2; dotted red: exposure 3. Error bars are shown only for the first exposure.

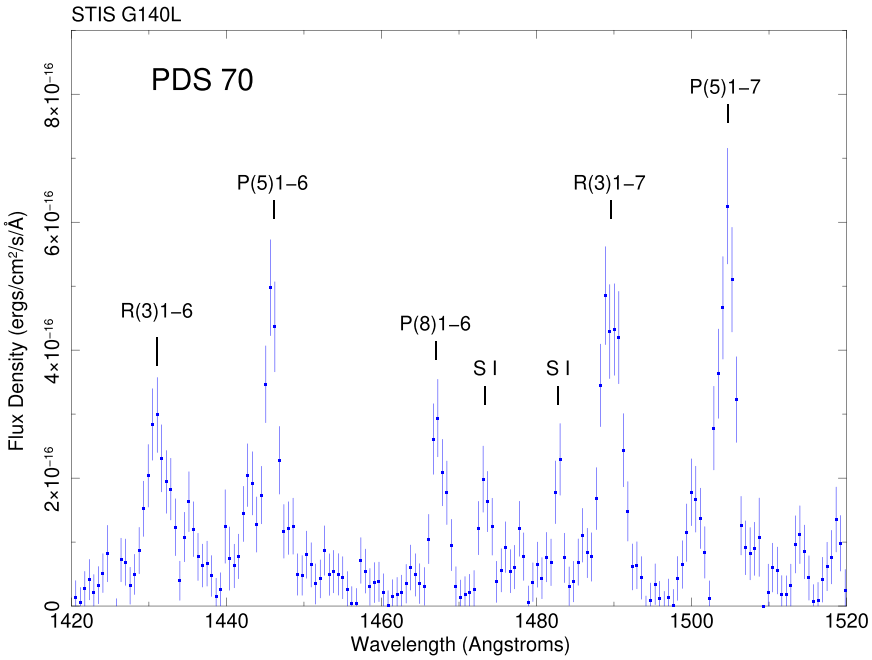

Figure 6. STIS/MAMA G140L spectrum of PDS 70 from combined exposures showing five prominent fluorescent H_2 lines. Tick marks show lab wavelengths of the H_2 transitions (Table 4). Weak neutral sulfur lines are marked at 1474 and 1483 Å.

or log $L_X = 29.80$ erg s^{-1}. Taking this latter value as representative For PDS 70 we obtain $L_X/L_* = 10^{-3.3}$, placing it close to the expected saturation boundary.

3.4. Density-sensitive Line Ratios

The flux ratios of density-sensitive lines can be used to estimate the electron density, n_e, in regions where the lines are formed. The derived densities are sensitive to several factors including abundances. However, if ratios of different lines of the same element are used the abundance uncertainty is avoided. Ratios of C III transitions have been used to estimate n_e in the solar atmosphere (Cook & Nicolas 1979, hereafter CN79) and in some cTTSs (Johns-Krull et al. 2000). This line forms at a maximum line power temperature log $T_{max} = 4.8$ (K), which is within the range of the solar transition region.

The FUV spectrum of PDS 70 shows C III lines at 1176.4 Å and 1908.7 Å but the C III line at 1247.4 Å is undetected (Table 3). Dereddening the 1176.4 and 1908.7 Å lines gives a

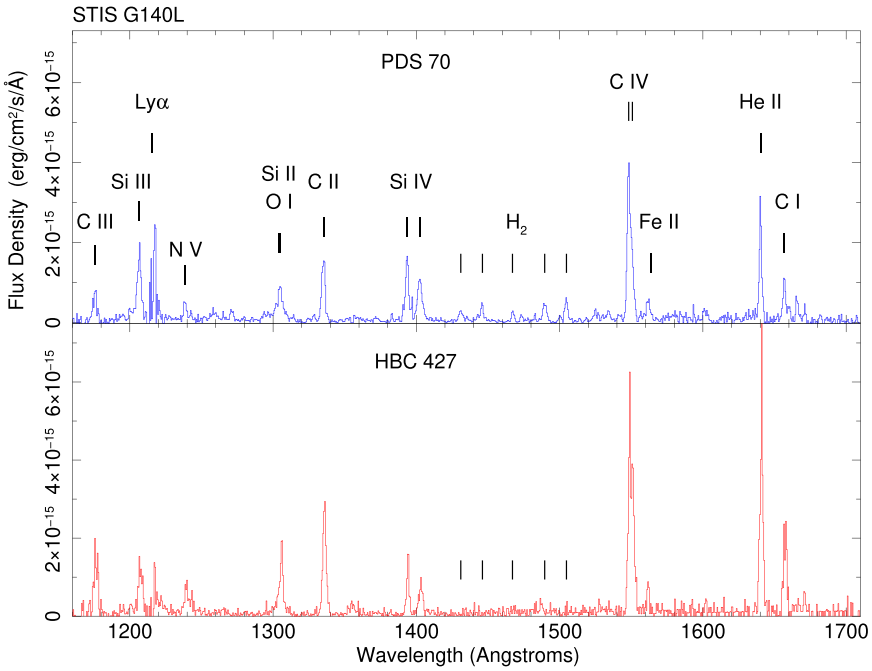

Figure 7. STIS/MAMA G140L spectra of PDS 70 and the K7e-type wTTS HBC 427 (=V397 Aur). The flux density of HBC 427 has been scaled up by a factor of 1.748 to correct for its greater distance (148.6 pc) than PDS 70 (112.39 pc). Error bars are not shown to facilitate comparison. The HBC 427 G140L archive spectrum (O8NS07020) is from a 1425 s observation on 2004 January 20 using the $52'' \times 0\farcs2$ slit. Note the lack of H_2 lines in the HBC 427 spectrum.

ratio $F_{\rm dered}(1176)/F_{\rm dered}(1908) = 0.50$. Assuming these lines form at or near $T_{\rm max}$ gives log $n_e = 8.5$ (cm^{-3}) using the results of CN79 evaluated on their log $T = 4.75$ curve. However, they note that the 1176/1908 line ratio underestimates n_e by about a factor of 5 relative to other line ratios. Applying a factor of 5 correction to the above gives log $n_e = 9.2$ (cm^{-3}). Again using the CN79 results the upper limit $F_{\rm dered}(1247)/F_{\rm dered}(1908) \leqslant 0.016$ gives log $n_e \leqslant 9.9$ (cm^{-3}). Densities in the above range $9.2 \leqslant$ log $n_e < 9.9$ (cm^{-3}) are typical of transition-region plasma (Doschek 1997) and provide confidence that the C III lines arise in the stellar atmosphere.

4. Discussion

4.1. PDS 70 Accretion Rate and Luminosity

Weak-lined T Tauri stars typically lack the accretion signatures commonly seen cTTSs such as UV continuum excesses, broadened high-temperature FUV lines (e.g., C IV), and fluorescent H_2 emission. As a representative case, Figure 7 shows that fluorescent H_2 lines are absent in the UV spectrum of the wTTS HBC 427. Nevertheless, some TTSs do show accretion signatures such as fluorescent H_2 emission even though other indicators are absent. These include RECX-11, which is thought to be accreting at a low rate $\dot{M}_{\rm acc} \leqslant 3 \times 10^{-10}\ M_\odot$ yr^{-1} (Ingleby et al. 2011; France et al. 2012).

The detection of FUV H_2 lines in PDS 70 supports previous claims that it is weakly accreting. To estimate the mass accretion rate we use the relation log $\dot{M}_{\rm acc}$ ($M_\odot$ yr^{-1}) $= (-5.4 \pm 0.2) + (0.8 \pm 0.1)$ log($L_{\rm CIV}/L_\odot$) given by Ardila et al. (2013). As a cautionary note, this relation was derived using a sample consisting mostly of cTTSs with considerable scatter in $\dot{M}_{\rm acc}$ and is not well calibrated at lower $L_{\rm CIV}$ values typical of wTTSs. We assume $A_V = 0.05$ (0.025–0.10) for PDS 70, allowing for a factor of 2 uncertainty. Dereddening the observed flux using this extinction gives $F_{\rm CIV,dered}(1548{+}1551) = 1.5$ (1.41–1.69) $\times 10^{-14}$ ergs cm^{-2} s^{-1} and log($L_{\rm CIV}/L_\odot$) $= -5.23$ (-5.25–5.18). The inferred accretion rate is then $\dot{M}_{\rm acc} = 2.6$ (0.5–14.8) $\times 10^{-10}$ $M_\odot$ yr^{-1} where the range in parentheses accounts for the uncertainties in A_V and the regression relation coefficients. The above range is consistent with the previous estimates of $\dot{M}_{\rm acc}$ obtained by Manara et al. (2019) and Thanathibodee et al. (2020) given in Section 1.

Based on an analysis of FUV spectra of a sample of 91 pre-main-sequence stars, Yang et al. (2012) obtained the following best-fit relation between $L_{\rm CIV}$ and accretion luminosity: log($L_{\rm CIV}/L_\odot$) $= -2.766{+}0.877$ log($L_{\rm acc}/L_\odot$). Using the same range of $L_{\rm CIV}$ values for PDS 70 as above that take A_V uncertainty into account, this relation gives log($L_{\rm acc}/L_\odot$) $= -2.81$ (-2.83 – -2.75) or $L_{\rm acc} = 5.93$ (5.66–6.80)$\times 10^{30}$ erg s^{-1}.

As a consistency check on the above we invoke the relation $L_{\rm acc} = \xi G \dot{M}_{\rm acc} M_*/R_*$, where $\xi = [1 - (R_*/r_i)]$ and r_i is the radius from which the accreting gas originates (Hartmann et al. 2016). Using the PDS 70 stellar parameters from Table 1 this becomes

$$\mathrm{L_{acc}} = \xi(7.3 \times 10^{30}) \left[\frac{\dot{M}_{\rm acc}}{10^{-10}\ M_\odot\ yr^{-1}} \right] \mathrm{erg\ s^{-1}}. \quad (1)$$

An additional constraint is that $r_i \leqslant r_{co} = 6.4\ R_*$ or, equivalently, $\xi \leqslant 0.844$, where $r_{\rm co}$ is the disk corotation radius for an assumed stellar rotation period $P_{\rm rot} = 3.03$ days (Thanathibodee et al. 2020). Combining this constraint with the above constraints on $\dot{M}_{\rm acc}$ and $L_{\rm acc}$ leads to the more restricted range $0.9 \leqslant [\dot{M}_{\rm acc}/10^{-10}\ M_\odot\ \mathrm{yr}^{-1}] \leqslant 1.1$ and $3.4 \leqslant r_i/R_* \leqslant 6.4$ (i.e., $0.705 \leqslant \xi \leqslant 0.844$). For comparison, the magnetospheric model of Thanathibodee et al. (2020) obtained a disk truncation radius $r_i/R_* = 4.0$, which lies within the above range.

4.2. Planet Irradiation by the Star

The disk gas model based on the ALMA observations of Keppler et al. (2019) leads to very high column densities at the

distance of the inner planet, effectively blocking stellar X-ray and UV radiation. The disk gas mass density in the midplane at a distance r from the star is $\rho(r) = 0.4\,\Sigma_{\rm gas}(r)/H(r)$, where $\Sigma_{\rm gas}(r)$ is the gas surface density and $H(r)$ the disk height radial profile (Equations [6] and [7] of Keppler et al. 2019).

Renormalizing the Keppler et al. (2019) results to a fiducial distance of $r = 1$ au gives $\Sigma_{\rm gas}(r) = \Sigma_0 r_{\rm au}^{-1}$ and $H(r) = H_0\, r_{\rm au}^{+1.25}$, where $\Sigma_0 \approx 10^2$ g cm^{-2}, $H_0 = 0.04$ au, and $r_{\rm au}$ is in units of au. We have neglected the exponential decay term in the expression for $\Sigma_{\rm gas}(r)$ used by Keppler et al. since it is near unity for small values of r in the inner disk where stellar X-ray and UV radiation are heavily absorbed. The adopted radial profile $\Sigma_{\rm gas}(r) \propto r^{-1}$ is only valid out to $r \approx$ 10–11 au, beyond which the gas density falls off much more rapidly in the gap (Figure 9 of Keppler et al. 2019). The behavior of $\Sigma_{\rm gas}(r)$ at $r \lesssim 5$ au is not well constrained observationally since this innermost region is not spatially resolved by ALMA. We thus leave Σ_0 as a free parameter below.

The disk gas number density is $n_{\rm H}(r) = \rho(r)/(\mu m_p)$, where m_p is the proton mass and we assume a mean molecular weight $\mu = 2.3$ (amu) for cold disk gas dominated by H and He in a ratio by number of H:He = 10 and H predominantly in molecular form as H_2. Integrating $n_{\rm H}(r)$ through the disk from inner radius r_i to outer radius r_f gives the equivalent neutral H column density $N_{\rm H} = \int_{r_i}^{r_f} n_{\rm H}(r){\rm d}r$. For X-ray photons of characteristic energy $E_X = {\rm k}T_X$ the optical depth is $\tau_X = \sigma(E_X)N_{\rm H}$, where $\sigma(E_X) = \sigma_0(E_X/1\ {\rm keV})^{-p}$ cm^2 is the X-ray photoelectric absorption cross section. We adopt $\sigma_0 = 2.27 \times 10^{-22}$ cm^2 and $p = 2.485$ (Igea & Glassgold 1999; Shang et al. 2002). For the X-ray photon energy $E_X \approx 1$ keV typical of PDS 70 in low-activity states the above gives unit optical depth $\tau_X = 1$ at $N_{\rm H} = 4.4 \times 10^{21}$ cm^{-2}.

Formally, the lower limit r_i on the integration to determine $N_{\rm H}$ should be taken as the inner truncation radius of the gas disk. This value is not well known but the estimates given above yield values of a few stellar radii, or much less than 1 au. Since $\Sigma_{\rm gas}(r)$ is not well determined close to the star, we set $r_{\rm in} = 5$ au for the integration. Then, integrating out to $r_f = 10$ au provides a *lower limit* on the absorption of X-rays by *pre-gap* disk gas.

Integrating with the above limits gives a column density $N_{\rm H}(r \leqslant 10\ {\rm au}) \geqslant 1.6 \times 10^{23}\ \Sigma_0$ cm^{-2}. In order for X-rays to penetrate this inner disk region ($\tau_X < 1$) a surface density $\Sigma_0 \lesssim 10^{-2}$ g cm^{-2} at $r = 1$ au is required. This is at least four orders of magnitude less than implied by the inner (unperturbed) disk gas model of Keppler et al. (2019). Thus, based on current knowledge of the disk gas profile as constrained by ALMA, the inner planet at $r = 22$ au is well-shielded from keV X-rays. The same conclusion holds for stellar UV radiation, which is more heavily absorbed than X-rays by virtue of its lower energy range and larger photoelectric absorption cross section (Bruderer et al. 2009).

4.3. Disk Photoevaporative Mass Loss and Dissipation

X-ray and UV (XUV) irradiation of disk gas leads to mass loss via a photoevaporative wind. This process, along with accretion onto the star (and planets, in the case of PDS 70) eventually depletes the disk gas and accretion ceases. X-ray, EUV, and FUV radiation can influence photoevaporative mass loss rates ($\dot{M}_{\rm pe}$) to varying degrees and detailed models must consider their relative importance. Theoretical estimates of $\dot{M}_{\rm pe}$ are sensitive to the adopted stellar and disk model parameters, the evolutionary state of the disk (i.e., early primordial disks versus evolved gapped disks), and to what degree relevant physical processes are included. Many physical processes can affect the disk temperature, density, and chemical distributions as reviewed by Woitke (2015). A key quantity entering into mass loss rate calculations is the disk gas surface density profile $\Sigma_{\rm gas}(r)$, which changes as the disk evolves (Figure 7 of Gorti et al. 2009). For most TTSs, including PDS 70, the behavior of $\Sigma_{\rm gas}(r)$ at small radii $r \lesssim 5$ au is not well constrained observationally due to limits on telescope angular resolution.

More than one study suggests that EUV radiation is less effective in driving gaseous disk evolution than X-ray or the combination of X-ray+FUV radiation (Gorti et al. 2009; Owen et al. 2012). Furthermore, the effects of FUV radiation are more important at early evolutionary stages when accretion rates are high and $L_{\rm FUV}$ is enhanced by accretion shocks (Gorti et al. 2009). Since PDS 70 is now only weakly accreting it is likely that X-ray radiation is the dominant factor driving its photoevaporative mass loss, although that was not necessarily the case at earlier stages.

Most models predict that the X-ray-driven mass loss rate $\dot{M}_{{\rm pe},x}$ scales nearly linearly with L_X and softer X-ray spectra lead to higher values of $\dot{M}_{{\rm pe},x}$, all other factors being equal (Ercolano et al. 2009; Gorti et al. 2009). This point is relevant to PDS 70 whose X-ray spectrum in low-activity states is quite soft for a wTTS, peaking near 1 keV and then falling off rapidly with negligible flux above 2 keV. Some accreting cTTSs, such as TW Hya, also have similar soft X-ray spectra (Kastner et al. 1999, 2002).

To obtain a rough estimate of the disk mass loss rate for PDS 70 we use the results of Alexander et al. (2006). Their formulation is appropriate for later stages of disk evolution when the inner disk is sufficiently cleared for direct stellar radiation to drive disk mass loss. This may be the case for the highly evolved PDS 70 disk but, as noted above, its disk gas surface density profile close to the star ($r \lesssim 5$ au) is not yet well constrained observationally.

Assuming the inner disk is sufficiently cleared to be directly affected by the star's ionizing radiation, the photoevaporative mass loss rate is (Equation (3) of Alexander et al. 2006)

$$\dot{M}_{\rm pe}(r < R_{\rm out}) = 9.69 \times 10^{-10} \mu C \left[\frac{H/R}{0.05}\right]^{-1/2} \left[\frac{R_{\rm in}}{3\ {\rm au}}\right]^{1/2} \left[\frac{\Phi}{10^{41}\ {\rm s}^{-1}}\right]^{1/2} M_\odot\ {\rm yr}^{-1}. \quad (2)$$

In the above we have used fiducial values given by Alexander et al. (2006) to compute the leading constant. The values of $R_{\rm in}$ and $R_{\rm out}$ are the inner and outer disk radii, μ is the mean mass per particle (amu), $C = [1 - (R_{\rm in}/R_{\rm out})^{0.42}]$, H/R is the ratio of disk scale height to radius, and Φ is the ionizing photon flux. As noted by Alexander et al., most of the mass loss occurs at radii near the gravitational radius, r_g, beyond which gas is no longer gravitationally bound to the star. Using $r_g = GM_*/c_s^2$ where $c_s \approx 10$ km s^{-1} is the sound speed assuming the escaping gas temperature is $T_{\rm gas} \sim 10^4$ K (Owen et al. 2012), gives $r_g \approx 7$ au for PDS 70. However, in hydrodynamic models the gas begins to escape at smaller radii and the effective value of r_g is reduced (e.g., Font et al. 2004). Thus, most of the mass loss for PDS 70 is expected to

occur inside 10 au. This is likely the case since the PDS 70 disk gas surface density falls off rapidly for $r > 10$ au in the gap. We thus take $R_{\rm out} = 10$ au for the mass loss calculation. The value of $R_{\rm in}$ is not well constrained but values in the range $R_{\rm in} = 1$–3 au yield similar mass loss rates and we adopt $R_{\rm in} = 1$ au. For PDS 70, the disk models of Keppler et al. (2019) give $(H/R) = 0.05$ at 3 au and $(H/R) = 0.07$ at 10 au so we just use the fiducial value $(H/R) = 0.05$ in the above equation.

For the ionizing photon flux Φ we include both EUV and X-ray emission, assuming $L_{\rm EUV} \approx L_X = 6 \times 10^{29}$ erg s^{-1}. Adopting mean photon energies $E_{\rm EUV} = 0.1$ keV and $E_X = 1$ keV gives $\Phi_{\rm EUV} = 3.75 \times 10^{39}$ s^{-1} and $\Phi_X = 3.75 \times 10^{38}$ s^{-1}. However, each primary X-ray photon spawns multiple secondary ionizations which effectively increase Φ_X. If $E_{\rm ion} \approx 0.037$ keV is the energy required to create an ion pair (Güdel 2015) then $E_X/E_{\rm ion} \approx 27$ and the adjusted ionization rate is $\Phi_X = 1.0 \times 10^{40}$ s^{-1}. We thus obtain $\Phi = \Phi_{\rm EUV} + \Phi_X = 1.375 \times 10^{40}$ s^{-1}. Inserting this into the above equation gives $\dot{M}_{\rm pe}(r < 10 \text{ au}) = 1.3 \times 10^{-10}\ \mu\ M_\odot$ yr^{-1}, where $\mu \approx 1.35$ for atomic gas and $\mu \approx 2.3$ for molecular gas. This mass loss rate is comparable to the PDS 70 mass accretion rate (Section 4.1). The value of $\dot{M}_{\rm pe}$ is not very sensitive to the assumed value of $L_{\rm EUV}$, which, as noted previously, is not observationally determined. If $L_{\rm EUV}$ is increased by a factor of 4 then $\dot{M}_{\rm pe}$ only increases by a factor of 1.35.

For comparison with the above, the studies of Ercolano et al. (2009) and Drake et al. (2009) focus on X-ray-driven mass loss and assume a disk that is in hydrostatic equilibrium and stellar parameters that are a reasonably close match for PDS 70. Their adopted X-ray spectrum includes soft emission $E_X < 1$ keV and assumes a mean temperature $\log T_X = 7.2$ K (k$T_X = 1.37$ keV), only slightly higher than for PDS 70 during low activity (k$T_X \approx$ 1 keV). The Drake et al. models consider a range of L_X values that brackets PDS 70. For $\log L_X = 29.8$ ergs s^{-1} their results give $\dot{M}_{{\rm pe},x} \approx 5 \times 10^{-10}\ M_\odot$ yr^{-1}. This is likely an overestimate for PDS 70 since their adopted disk model assumes a surface density profile $\Sigma(r)$ with a smooth power-law decline based on D'Alessio et al. (1998), whereas the PDS 70 disk is heavily perturbed with a wide low-surface-density gap centered near 22 au. Taking the likelihood of an overestimate into account, the predicted mass loss rate of Drake et al. may not differ much from that based on the formulation of Alexander et al. (2006) given above, that is, $\dot{M}_{\rm pe} \sim 10^{-10}\ M_\odot$ yr^{-1}. But other studies, such as the hydrodynamic mass loss models of generic disks described by Owen et al. (2012), predict mass loss rates an order of magnitude larger than above. Taken together, these results suggest $\dot{M}_{\rm pe} \gtrsim \dot{M}_{\rm acc}$ for PDS 70. In this case disk mass loss competes with or even starves accretion, as discussed by Drake et al. (2009).

4.4. Disk Lifetimes

The predicted disk lifetime from theoretical models depends on several factors including the assumed initial (primordial) disk mass and viscosity. As such, disk lifetime predictions are heavily model dependent. Other relevant factors are binarity and environmental effects such as OB star winds and strong UV radiation fields in massive star-forming regions. To briefly summarize previous work, the models of Alexander et al. (2006) predict $t_{\rm disk} \sim$ 6–8 Myr for an assumed ionizing flux $\Phi = 10^{42}$ s^{-1}, significantly higher than PDS 70 at current epoch. The study of Gorti et al. (2009) considered the combined effects of X-ray, EUV, and FUV radiation and obtained $t_{\rm disk} \sim$ 2–6 Myr. The lower value corresponds to a soft X-ray spectrum with significant emission below 1 keV and stronger photoevaporation than harder spectra. Their predictions assumed $\log L_X = 30.3$ erg s^{-1}, about 3 times larger than PDS 70 at the current epoch. The empirical study of Bertout et al. (2007), based on derived ages of TTSs in Taurus-Auriga, obtained an average disk lifetime $t_{\rm disk} = 4(M_*/M_\odot)^{0.75}$ Myr. Their model does take mass accretion into account but not photoevaporation. A similar study of the Lupus association by Galli et al. (2015) deduced an average lifetime $t_{\rm disk} = 3(M_*/M_\odot)^{0.55}$ Myr. Average disk lifetimes for specific star-forming regions provide a useful reference but significant variation can also be present. The study of Taurus-Auriga disks by Armitage et al. (2003) reveals a large dispersion in disk lifetimes. Most disks have dissipated at stellar ages of ~6 Myr but some survive longer. The reason for the large dispersion is not known but variations in initial disk mass is one possible explanation.

The above results span a rather large range but suggest that most TTS disks do not survive longer than ~6 Myr, the estimated age of PDS 70 (Table 1). We thus conclude that the PDS 70 disk is near the end of its expected lifetime and in the final stages of being cleared. PDS 70 thus serves as a rare example of the terminal stage of TTS disk evolution and as the host star of a formative planetary system.

5. Summary

HST STIS FUV and NUV spectra of PDS 70 reveal emission lines formed at chromospheric and transition-region temperatures. Stellar continuum is detected but any weak FUV continuum excess that might be present from accretion shocks is of low significance. The detection of several FUV fluorescent H_2 lines provides evidence for molecular gas in the vicinity of the star that is potentially feeding weak accretion as the inner disk drains. XUV irradiation of the remaining disk gas is predicted to be driving a weak photoevaporative disk wind whose mass loss rate is comparable to or greater than the inferred accretion rate $\dot{M}_{\rm pe} \gtrsim \dot{M}_{\rm acc} \sim 10^{-10}\ M_\odot$ yr^{-1}. The combined effects of photoevaporation and residual accretion onto the star and planets portend the approaching end of the disk's lifetime. As the disk clears the planets will be more directly exposed to the star's ionizing radiation.

This work was supported by HST award HST-GO-16290 issued by the Space Telescope Science Institute (STScI) and is based on observations made with the NASA/ESA Hubble Space Telescope, operated by the Association of Universities for Research in Astronomy, Inc. under contract with NASA. This work has utilized data in the XMM-Newton Science Archive and data analysis products including STSDAS and PyRAF produced by the STScI, and HEASOFT developed and maintained by HEASARC at NASA GSFC.

Facilities: Hubble Space Telescope (STIS).

ORCID iDs

Stephen L. Skinner https://orcid.org/0000-0002-3025-3055
Marc Audard https://orcid.org/0000-0003-4721-034X

References

Abgrall, H., Roueff, E., Launay, F., Roncin, J.-Y., & Subtil, J.-L. 1993, A&AS, 101, 273
Alexander, R. D., Clarke, C. J., & Pringle, J. E. 2006, MNRAS, 369, 229
Ardila, D. R., Basri, G., Walter, F. M., Valenti, J. A., & Johns-Krull, C. M. 2002, ApJ, 566, 1100
Ardila, D. R., Herczeg, G. J., Gregory, S. G., et al. 2013, ApJS, 207, 1
Armitage, P. J., Clarke, C. J., & Palla, F. 2003, MNRAS, 342, 1139
Bergin, E., Calvet, N., Sitko, M. L., et al. 2004, ApJ, 614, L133
Bertout, C., Siess, L., & Cabrit, S. 2007, A&A, 473, L21
Bruderer, S., Doty, S. D., & Benz, A. O. 2009, ApJS, 183, 179
Christiaens, V., Cantalloube, F., Casassus, S., et al. 2019, ApJL, 877, L33
Cook, J. W., & Nicolas, K. R. 1979, ApJ, 229, 1163
D'Alessio, P., Cantó, J., Calvet, N., & Lizano, S. 1998, ApJ, 500, 411
Doschek, G. A. 1997, ApJ, 476, 903
Drake, J. J., Ercolano, B., Flaccomio, E., & Micela, G. 2009, ApJ, 699, L35
Ercolano, B., Clarke, C. J., & Drake, J. J. 2009, ApJ, 699, 1639
Font, A. S., McCarthy, I. G., Johnstone, D., & Ballantyne, D. R. 2004, ApJ, 607, 890
France, K., Schindhelm, E., Bergin, E. A., Roueff, E., & Abgrall, H. 2014, ApJ, 784, 127
France, K., Schindhelm, E., Herczeg, G. J., et al. 2012, ApJ, 756, 171
France, K., Yang, H., & Linsky, J. L. 2011, ApJ, 729, 7
Galli, P. A. B., Bertout, C., Teixeira, R., & Ducourant, C. 2015, A&A, 580, 26
Gorti, U., Dullemond, C. P., & Hollenbach, D. 2009, ApJ, 705, 1237
Gregorio-Hetem, J., & Hetem, A., Jr. 2002, MNRAS, 336, 197
Güdel, M. 2015, EPJWC, 102, 00015
Güdel, M., Guinan, E. F., & Skinner, S. L. 1997, ApJ, 483, 947
Haffert, S. Y., Bohn, A. J., de Boer, J., et al. 2019, NatAs, 3, 749
Hartmann, L., Herczeg, G., & Calvet, N. 2016, ARA&A, 54, 135
Herczeg, G. J., Linsky, J. L., Walter, F. M., Gahm, G. F., & Johns-Krull, C. M. 2006, ApJS, 165, 256
Igea, J., & Glassgold, A. E. 1999, ApJ, 518, 848
Ingleby, L., Calvet, N., Bergin, E., et al. 2011, ApJ, 743, 105
Ingleby, L., Calvet, N., Herczeg, G., et al. 2013, ApJ, 767, 112
Isella, A., Benisty, M., Teague, R., et al. 2019, ApJL, 879, L25
Johns-Krull, C. M., Valenti, J. A., & Linsky, J. L. 2000, ApJ, 539, 815
Joyce, S. R. G., Pye, J. P., Nichols, J. D., et al. 2020, MNRAS, 491, L56
Kastner, J. H., Huenemoerder, D. P., Schulz, N. S., Canizares, C. R., & Weintraub, D. A. 2002, ApJ, 567, 434
Kastner, J. H., Huenemoerder, D. P., Schulz, N. S., & Weintraub, D. A. 1999, ApJ, 525, 837
Keppler, M., Benisty, M., Müller, A., et al. 2018, A&A, 617, A44
Keppler, M., Teague, R., Bae, J., et al. 2019, A&A, 625, A118
Kiraga, M. 2012, AcA, 62, 67
Kravtsova, A. S., & Lamzin, S. A. 2003, AstL, 29, 612
Long, Z. C., Akiyama, E., Sitko, M., et al. 2018, ApJ, 858, 112
Manara, C. F., Mordasini, C., Testi, L., et al. 2019, A&A, 631, L2
Müller, A., Keppler, M., Henning, Th., et al. 2018, A&A, 617, L2
Owen, J. E., Clarke, C. J., & Ercolano, B. 2012, MNRAS, 422, 1880
Pecaut, M. J., & Mamajek, E. E. 2016, MNRAS, 461, 794
Ribas, I., Guinan, E. F., Güdel, M., & Audard, M. 2005, ApJ, 622, 680
Sanz-Forcada, J., Micela, G., Ribas, I., et al. 2011, A&A, 532, A6
Schneider, P. C., Eislöffel, J., Güdel, M., et al. 2013a, A&A, 550, L1
Schneider, P. C., Eislöffel, J., Güdel, M., et al. 2013b, A&A, 557, A110
Shang, H., Glassgold, A. E., Shu, F. H., & Lizano, S. 2002, ApJ, 564, 853
Skinner, S. L., Schneider, P. C., Audard, M., & Güdel, M. 2018, ApJ, 855, 143
Thanathibodee, T., Molina, B., Calvet, N., et al. 2020, ApJ, 892, 81
Tu, L., Johnstone, C. P., Güdel, M., & Lammer, H. 2015, A&A, 577, L3
Whittet, D. C. B., Shenoy, S. S., Clayton, G. C., & Gordon, K. D. 2004, ApJ, 602, 291
Woitke, P. 2015, EPJWC, 102, 00011
Wood, B. E., Redfield, S., Linsky, J. L., Müller, H.-R., & Zank, G. P. 2005, ApJS, 159, 118
Yang, H., Herczeg, G. J., Linsky, J. L., et al. 2012, ApJ, 744, 121
Youngblood, A., Pineda, J. S., Ayres, T., et al. 2022, ApJ, 926, 129
Zhou, Y., Bowler, B. P., Wagner, K. R., et al. 2021, ApJ, 161, 244